Chapter 5

Nanoscale Conductivity of LB Films of PyTp and PyTp - DNA Complex Studied by Current-Sensing Atomic Force Microscopy

5.1 Introduction

Discotic mesogens (discogens) are promising materials for organic electronics [1]. They possess unique molecular electronic features, particularly the two-dimensional delocalization of electrons, that are not observed in linear oligomers and polymers. The two-dimensional delocalization of electrons (i.e., in the x,y plane of the discogen molecules and in the z-direction of the column axis) presents unusual aspects; (i) low band gap and low reorganization energies associated with chemical stability in ambient conditions, (ii) high charge carrier mobility for electrons even in the presence of water and oxygen, (iii) high sensitivity of charge transport to structural defects and dynamics due to its quasi one-dimensional character, and (iv) bandwidth comparable to that of graphite. In addition, these molecular electronic properties are amplified at the supramolecular level due to the extended interactions between the delocalized π-orbitals of the discotic molecules. These intrinsic electronic properties combined with their trend to form large ordered domains make them potential candidates for fabrication of devices like field-effect transistors, photovoltaic cells and light-emitting diodes. Compared to these conventional discogens, ionic discogens are even more interesting due to the presence of ions as charge carriers [2, 3]. The ionic discogens find application in designing anisotropic ion-conductive materials [4].

In the previous chapters, we have shown that the PyTp molecule, which is a cationic discogen,

can form stable complex with DNA at the air-water (A-W) interface. Interestingly, the PyTp-DNA complex film can be successfully transferred onto substrates to form multilayers [5] which opens scope for various device applications. Our studies on the mechanical properties of these films at nanoscale have shown that the PyTp-DNA complex film is much rigid than the pure PyTp film. Out of the many possible applications mentioned in the last chapter, the application of such a system in molecular electronic devices is the most promising one [6–8]. The DNA molecule has drawn lot of attention in nanoelectronic devices due to its intrinsic electronic properties [9, 10]. The charge-transfer reactions and conductivity measurements show a large variety of possible electronic behavior, ranging from Anderson and band-gap insulators to effective molecular wires [11]. Since both DNA and discogens have their own intrinsic electronic properties, complexing DNA with cationic discogen molecules is a novel approach for developing advanced materials with interesting electronic properties.

In literature, the studies on aliphatic lipid-DNA complexes are mostly aimed to reveal supramolecular structures for nonviral gene delivery [12]. There are only a few efforts for using such systems in organic electronics since aliphatic lipids are not good candidate for electron transport. However, Okahata et al. have reported anisotropic electrical conductivity in LB films of aliphatic lipid-DNA complex [13] where the DNA molecules were aligned in the film deposition direction. Their measurements were carried out at macroscopic length scale and they showed that the conductivity was 10^4 times more in the direction parallel to the aligned DNA strands as compared to the direction perpendicular to it. Although these aliphatic lipid-DNA complexes are known for decades, the discogen-DNA complexes have been studied recently [14] and these are expected to have some novel molecular electronic properties. However, no electrical conductivity measurements at molecular level have previously been reported on such films.

To study electron conduction at molecular level, scanning probe techniques (scanning tunneling microscope (STM) and current sensing atomic force microscope (CS-AFM)) are the most suitable methods [15,16]. CS-AFM provides an attractive approach to make electrical contact with a monolayer film under controlled load. Such a contact leads to the formation of metal-molecule-metal junction [17]. Further, in CS-AFM, the images of topography and current are simultaneously ob-

tained, enabling direct correlation of local topography with electrical properties at nanoscale [18]. The conventional CS-AFM operates in contact mode. For soft systems, the damage due to the lateral shear forces in contact mode imaging is an important issue. Recently, Casuso et al. have introduced a novel methodology and performed the conductivity maps in jumping mode, rather than in contact mode for biomembranes [19]. However, for systems which are not very soft like self-assembled monolayer and polymers, the contact mode can still be used [17, 20].

In this chapter, we present electrical conductivity measurements at nanoscale on Langmuir-Blodgett (LB) films of pure PyTp monolayer and PyTp-DNA complex monolayer employing CS-AFM. Our measurements show that the conductivity of PyTp-DNA complex film is much less compared to the pure PyTp film. The ability to rationally design molecular electronic components hinges on a fundamental understanding of the charge transport mechanism in metal-molecule-metal junctions. To this end, we look for a possible mechanism for electron transport at nanoscale in our metal-LB film-metal system. The analysis of the current-voltage (I-V) curves suggests that the electron transport mechanism in our system follows the Fowler-Nordheim tunneling model.

5.2 Experiment

The pure PyTp and PyTp-DNA complex films were prepared as described in Chapter 2 and 3. The films were compressed to a target surface pressure of 35 mN/m and then these films were transferred from the air-water (A-W) interface to solid substrates by LB technique. We have used two types of substrates for film deposition; gold coated mica and polished doped silicon. The gold coated mica substrates, which are hydrophilic, were obtained from Molecular Imaging, USA. These substrates were very clean and hence they were just rinsed with HPLC grade chloroform and ultra pure deionized water, before film deposition. The silicon substrates were double sided mirror polished, boron doped with resistivity $\sim$ 0.0005 Ohm-cm and <100> orientation, obtained from AppNano, USA. To make the surface hydrophilic, the silicon substrates were dipped in hot piranha solution (mixture of concentrated H_2SO_4 and H_2O_2 in 3:1 ratio) for about 5 minutes and then rinsed thoroughly with ultra pure deionized water, before film deposition. Conductivity measurements were carried out using a contact mode CS-AFM (model PicoPlus, Molecular Imaging). We have

used platinum coated silicon cantilevers (probe model: ANSCM-PC, AppNano, USA) having spring constant in the range of 0.02 to 0.8 N/m, tip radius ~ 30 nm and resonance frequency in the range of 5 to 25 kHz for CS-AFM measurements. The conductive tip behaves effectively as a metal electrode with an area mainly determined by the tip-sample contact region. With the tip at virtual ground, a selectable bias voltage is applied between the tip and the sample. A preamplifier, with a sensitivity of 1 nA/Volt and operational range from 1 pA to 10 nA was used. In our CS-AFM apparatus, the rms noise level was about 2 pA and any signal above this value was detectable. The deflection of the cantilever was monitored and kept constant to maintain a constant force between the tip and sample, and simultaneous topographic and current images were generated. During *I-V* measurements, the feedback loop was enabled, meaning that the force applied by the cantilever was held constant. All the *I-V* measurements were performed on gold substrates by placing the tip at the desired position on the film and carefully selecting the force. In addition, after every *I-V* measurements, we have scanned the same region to ensure no damage to the film. All measurements were carried out in ambient conditions at a temperature of 25^0 C and relative humidity ~30 %.

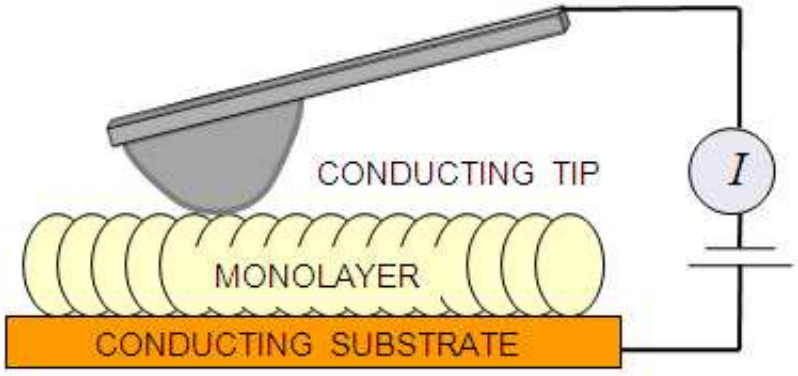

Figure 5.1: Schematic representation of a metal-molecule-metal junction formed by a conducting AFM tip in contact with a monolayer film deposited on a conducting substrate.

An advantage of CS-AFM is the experimental simplicity, providing a convenient alternative to labor intensive microfabrication methods for making metal-molecule-metal junction (Figure 5.1). Unlike STM, in CS-AFM the probe is positioned using normal force feedback, which decouples probe positioning from the sample conductivity [21]. Hence, the surface topography of the film

and its electrical conductivity can be acquired simultaneously and independently. Thus, CS-AFM is a promising approach for studying transport through molecular junctions [22].

5.3 Theory

5.3.1 Models for Electron Transport Through Metal-Insulator-Metal Junction

We consider two metallic electrodes separated by an insulating film forming a metal-insulator-metal (M-I-M) junction. The equilibrium conditions require that the top of the energy gap of the insulator be positioned above the Fermi level of the electrodes. The action of the insulating film is to introduce a potential barrier between the electrodes which impedes the flow of electrons between the electrodes. The potential barrier extends from the electrode Fermi level to the bottom of the insulator conduction band. There are two basic mechanisms for electron transport through the insulating region between the two electrodes; thermionic emission (Schottky emission) and electron tunneling. Thermionic emission occurs when electrons have enough energy to pass over the potential barrier. When electrons do not have sufficient energy, tunneling is the main mechanism for electron transport across the potential barrier. In this section, we present a brief review of the models for these two mechanisms. We will explore how these models can be used to account for the measured *I*-*V* curves and to determine the barrier height between the conducting tip and sample.

5.3.1.1 Schottky Emission

Schottky emission is usually used to explain the conductivity through a metal-semiconductor interface [23]. The potential barrier, which forms when a metal makes contact with a semiconductor, arises from the separation of charges at the metal-semiconductor interface such that a region depleted of mobile carriers is created in the semiconductor (Figure 5.2). In the most simple case, the barrier height is given by the difference of work functions of the metal and semiconductor. The current through the interface is controlled by two processes; first, thermionic emission over the barrier and second, drift and diffusion in the depletion region. The following current (*I*)-voltage

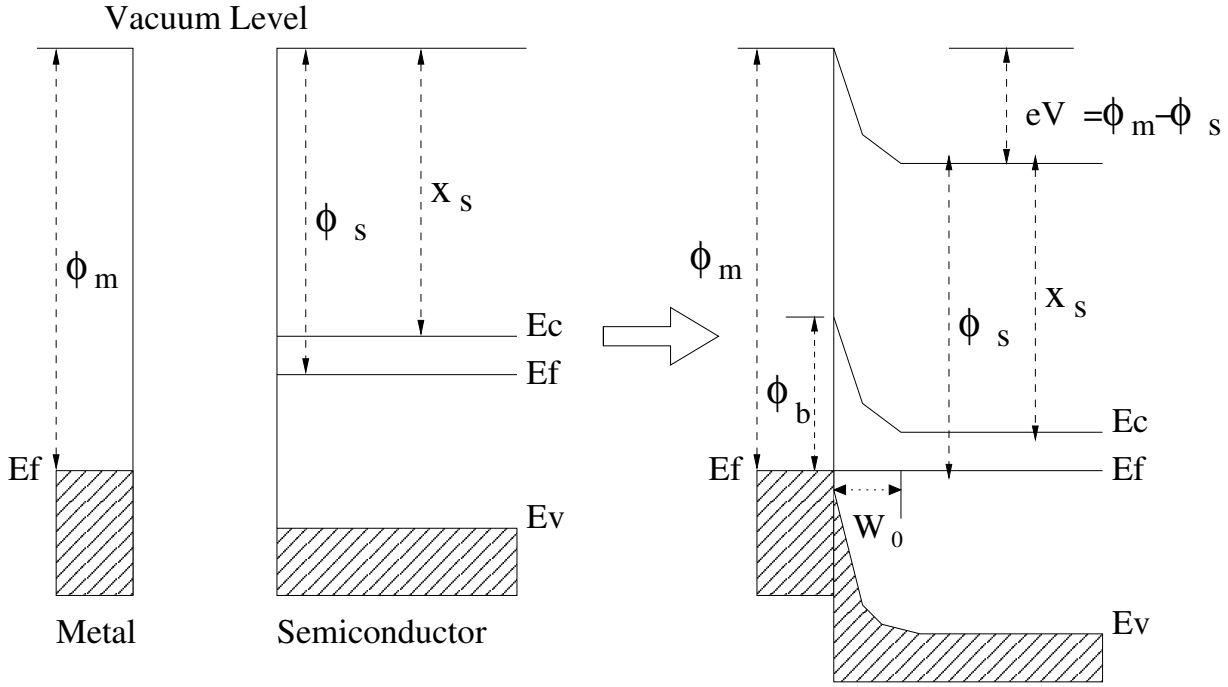

Figure 5.2: Energy band diagrams of metal contact to n-type semiconductor. The Schottky barrier height $\phi_b = \phi_m - \phi_s + Ec - Ef$. ϕ_m and ϕ_s are the work functions of the metal and the semiconductor respectively. Ef is the Fermi energy. V is the applied voltage. X_s is the electron affinity. Ec is the lowest electron energy in the conduction band and Ev is the highest electron energy in the valance band. W_0 is the width of the depletion layer.

(V) expression (Schottky diode equation) results from this model:

$$I(V) = C[\exp(-DV) - 1], \tag{5.1}$$

where,

$$C = SRT^2 \exp\left(-\frac{\phi_b}{k_B T}\right), \tag{5.2}$$

and

$$D = \frac{e}{k_B T}. \tag{5.3}$$

In these expressions, S is the contact area, T is temperature, k_B is Boltzman constant, ϕ_b is barrier height, e is electron charge and R is given by

$$R = \frac{4\pi m^* e k_B^2}{h^3}. \tag{5.4}$$

Here, m^* is the effective mass of electron, h is Planck's constant.

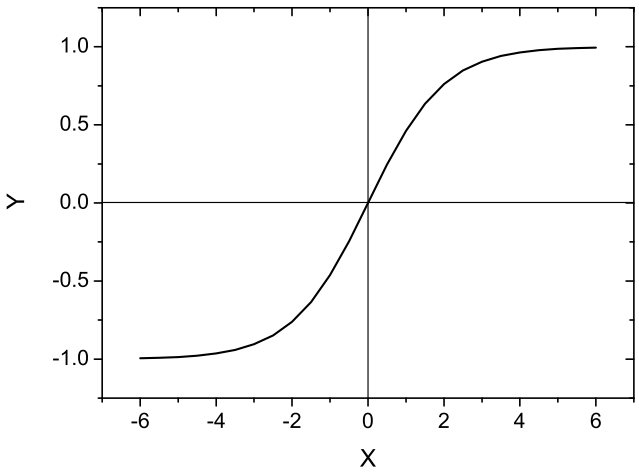

Figure 5.3: The functional form of Y = [exp(X)-1]/[exp(X)+1]

Schottky emission equation can also be used to explain the current through M-I-M junction. For our metal-LB film-metal junction, if we apply the Schottky emission model, there will be two Schottky junctions in series. One is forward biased and the other is reverse biased. We assume one to be forward biased with voltage V_1 and the other to be reverse biased with voltage V_2. Also, we assume the contact area between the LB film and the AFM tip and the contact area between the LB film and the gold substrate to be the same, then:

$$I = C\left(\exp\left(\frac{eV_1}{k_BT}\right) - 1\right) = C\left(1 - \exp\left(-\frac{eV_2}{k_BT}\right)\right) \tag{5.5}$$

Since V_1+V_2=V, we obtain the equation:

$$I = C\frac{\exp\left(\frac{eV}{k_BT}\right) - 1}{\exp\left(\frac{eV}{k_BT}\right) + 1} \tag{5.6}$$

The functional form of this equation is shown in Figure 5.3. It can be seen that for thermionic emission in a M-I-M junction, the derivative dI/dV decreases with increasing current. The I-V curves measured by CS-AFM for a M-I-M junction can be fitted with equation 5.6 to determine the value of C. Using this C value, we can obtain the barrier height ϕ_b (in the unit of eV) from the following expression:

$$\phi_b = k_BT\ln(A_{eff}RT^2/C) \tag{5.7}$$

where A_{eff} is the effective contact area between the AFM tip and the sample surface.

5.3.1.2 Tunneling Models

Tunneling is purely a quantum mechanical phenomenon. During the tunneling process, a particle can penetrate through a barrier (i.e., a classically forbidden region) and transfer from one classically allowed region to another. This happens because particles also have wave characteristics. Since the development of quantum mechanics, tunneling phenomenon has been studied by both theorists and experimentalists on many different systems. One of the extensively studied tunneling structures is the metal-insulator-metal (M-I-M) junction. If two metal electrodes are separated by an insulating film, and the film is sufficiently thin, current can flow between the two electrodes by means of tunneling. The purpose of this insulating film is to introduce a potential barrier between the metal electrodes. The energy band diagrams of M-I-M junction with similar metal electrodes are shown in Figure 5.4 under three biasing conditions.

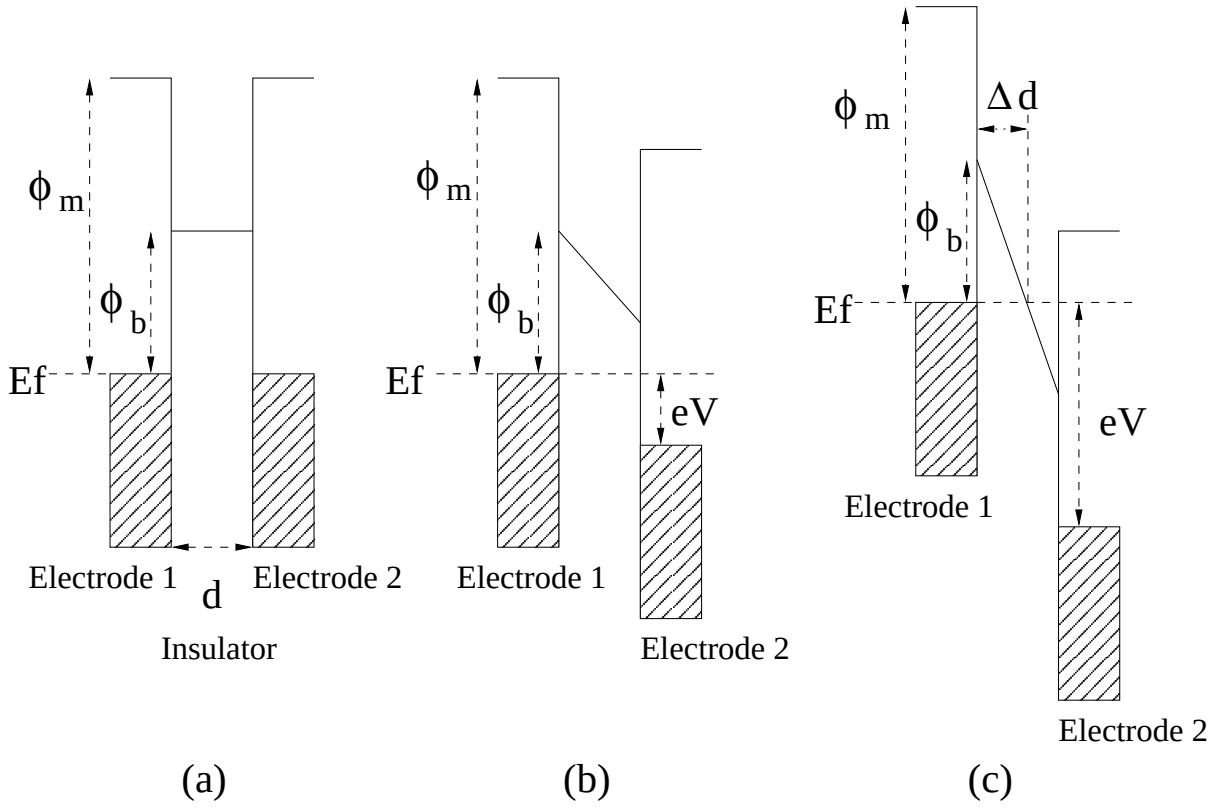

Figure 5.4: Rectangular potential barrier in a metal-insulator-metal junction. (a) V=0; (b) V<ϕ_b/e; (c) V>ϕ_b/e. V is the applied voltage to the junction. Ef is the Fermi energy of the metal. ϕ_b is the barrier height between the metal and the insulator. d is the separation distance between the two electrodes.

Simmons derived a generalized formula for the tunneling current through a potential barrier of arbitrary shape existing in a M-I-M junction [24]. For simplicity, we consider a rectangular potential barrier as shown in Figure 5.4. The simplest way to model the current-voltage behavior of such a junction within the Simmons approximation is given by the following equation:

$$I = A\left\{\left(\phi_b - \frac{eV}{2}\right)\exp\left[-B\left(\phi_b - \frac{eV}{2}\right)^{1/2}\right] - \left(\phi_b + \frac{eV}{2}\right)\exp\left[-B\left(\phi_b + \frac{eV}{2}\right)^{1/2}\right]\right\} \tag{5.8}$$

where,

$$A = \frac{A_{eff}\, e}{2\pi h d^2} \tag{5.9}$$

$$B = \frac{4\pi d\,\sqrt{2m^*}}{h} \tag{5.10}$$

Equation 5.8 was derived for a symmetric M-I-M system, assuming a linear voltage drop inside the insulator and neglecting space charge and image charge effects. Here, A_{eff} is the effective contact area, V is the applied voltage, d is the separation between the two electrodes (i.e., barrier width) and ϕ_b is the contact barrier height. e , m^* and h are electron charge, effective mass of the electron, and Planck's constant respectively. In molecular junctions, the barrier width corresponds to the molecular length, and the barrier height can be approximated by the energy offset between the electrode Fermi level and the nearest molecular orbital level.

After a bias voltage is applied, the shape of a rectangular barrier changes to a trapezoidal shape for V<ϕ_b/e (Figure 5.4(b)). Tunneling through a trapezoidal barrier is called direct tunneling because the charge carriers are injected directly into the electrode. In this regime, equation 5.8 reduces to

$$I \approx \left(\frac{A_{eff}e^2(2m^*\phi_b)^{1/2}}{h^2 d}\right)V\,\exp\left[-\frac{4\pi d(2m^*\phi_b)^{1/2}}{h}\right] \tag{5.11}$$

which indicates that the tunneling current increases linearly with the applied bias. It also shows that the current depends on the barrier width exponentially.

However, when the applied bias voltage is larger than the barrier height (V>ϕ_b/e), the barrier shape further changes from trapezoidal to a triangular barrier (Figure 5.4(c)). Tunneling through a triangular barrier, where the carriers tunnel into the conduction band of the insulator, is called Fowler-Nordheim tunneling or field emission [25]. In this high voltage regime, equation 5.8 reduces to

$$I(V) = A\,V^2 \exp\left(-\frac{B}{V}\right) \tag{5.12}$$

where A and B are given by;

$$A = \frac{A_{eff} e^3 m^*}{8\pi h \phi_b d^2 m} \tag{5.13}$$

$$B = \frac{8\pi\sqrt{2m^*}\phi_b^{3/2}}{3he} = 6.83\,d\left(\frac{m^*}{m}\right)^{1/2}\phi_b^{3/2}(Volts) \tag{5.14}$$

Here, the units of d and ϕ_b are nm and eV respectively. To extract meaningful information from the high-voltage regime, it is useful to linearize the equation 5.12;

$$ln\left(\frac{I}{V^2}\right) \propto -B\left(\frac{1}{V}\right) \tag{5.15}$$

From equation 5.15, it is obvious that a plot of $\ln(I/V^2)$ against $1/V$ will yield a straight line, the slope of which will depend on the barrier height. Since we can not determine the effective contact area, the constant A (equation 5.13) is not very useful in our system. Hence, we determine the constant B (equation 5.14), from which we can evaluate the barrier height ϕ_b.

5.4 Results

The monolayer films of both pure PyTp and PyTp-DNA complex were transferred onto gold coated mica substrates at a target surface pressure of 35 mN/m by LB technique. At this surface pressure, the molecules arrange themselves in an edge-on configuration (as shown in Chapter 2). Prior to performing the current imaging and I-V measurements on these LB films, we have tested the

conductivity of the current-sensing AFM tip by performing *I-V* spectroscopy with a platinum coated tip in contact with a bare gold surface. Figure 5.5 shows the *I-V* characteristics measured on a bare gold surface at a constant force of 4 nN. The measured *I-V* curve was a straight line whose slope yielded a value of nearly 100 MΩ for the contact resistance.

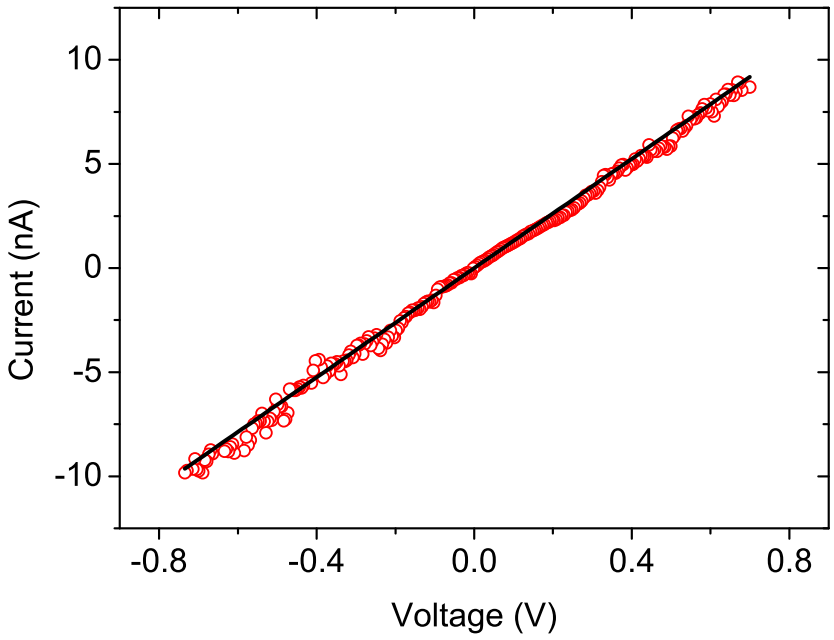

Figure 5.5: Current vs voltage characteristics measured for a bare gold surface coated on mica substrate at a constant force of 4 nN. The open circles represent the experimental data points. The solid line represents a straight line fit to the experimental data points. The slope yields a value of nearly 100 MΩ for the contact resistance.

Additionally, we have obtained topography (Figure 5.6(a)) and current (Figure 5.6(b)) images for the bare gold film coated on mica. The topography image shows small step-like features which is due to the steps present on the cleaved mica surface. The current image shows inhomogeneity in current flow across the surface. This inhomogeneity might be due to the defects in gold coating on mica substrate. Since the platinum coating on the AFM tips are very delicate, they can be damaged and lose its conductivity for high current and high load conditions. Hence, in all our *I-V* measurements and current imaging, we limited the tip current to less than 10 nA and the contact force between the tip and the sample to less than 10 nN.

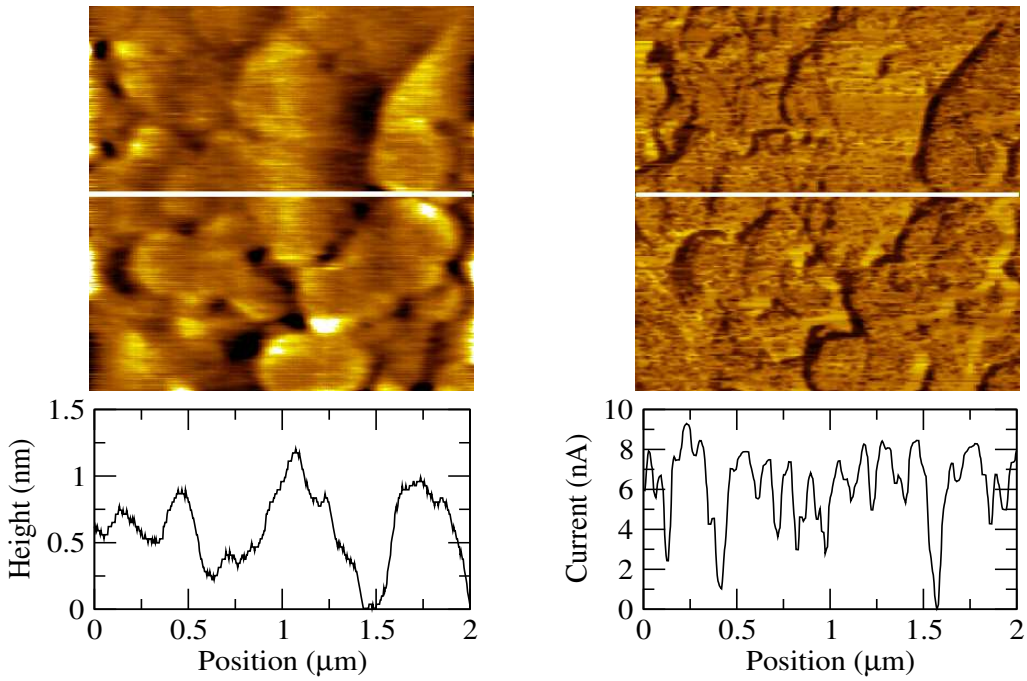

(a) (b)

Figure 5.6: CS-AFM images of a bare gold film on a mica substrate at a constant force of 4 nN: (a) Topography. (b) Current image at 0.5 V sample bias.

5.4.1 Current Imaging by contact mode CS-AFM

The PyTp monolayer film was deposited on gold coated mica substrate by LB technique and were imaged by contact mode CS-AFM. By maintaining a constant force of 4 nN between the tip and sample, simultaneous topographic and current images were obtained for sample bias voltages of 0.1, 1 and 2 Volts (Figure 5.7). The topography shows a film height ~ 2.2 nm with respect to a small void (Figure 5.7(a)). This value is expected for the molecules in an edge-on configuration. The steps observed on the surface corresponds to the steps on the mica surface. At a sample bias of 0.1 Volt, there was negligible current except for the small void region (Figure 5.7(b)). This was within the error bar and hence not measurable. Therefore, the current image at this bias voltage did not reveal any features. For the sample bias voltage of 1 Volt, a current flow in the range of 0.1 to 0.4 nA was observed. The current flow was further increased by increasing the sample bias voltage to 2 Volts.

In order to resolve the features in the current image, we have scanned the film at smaller scan

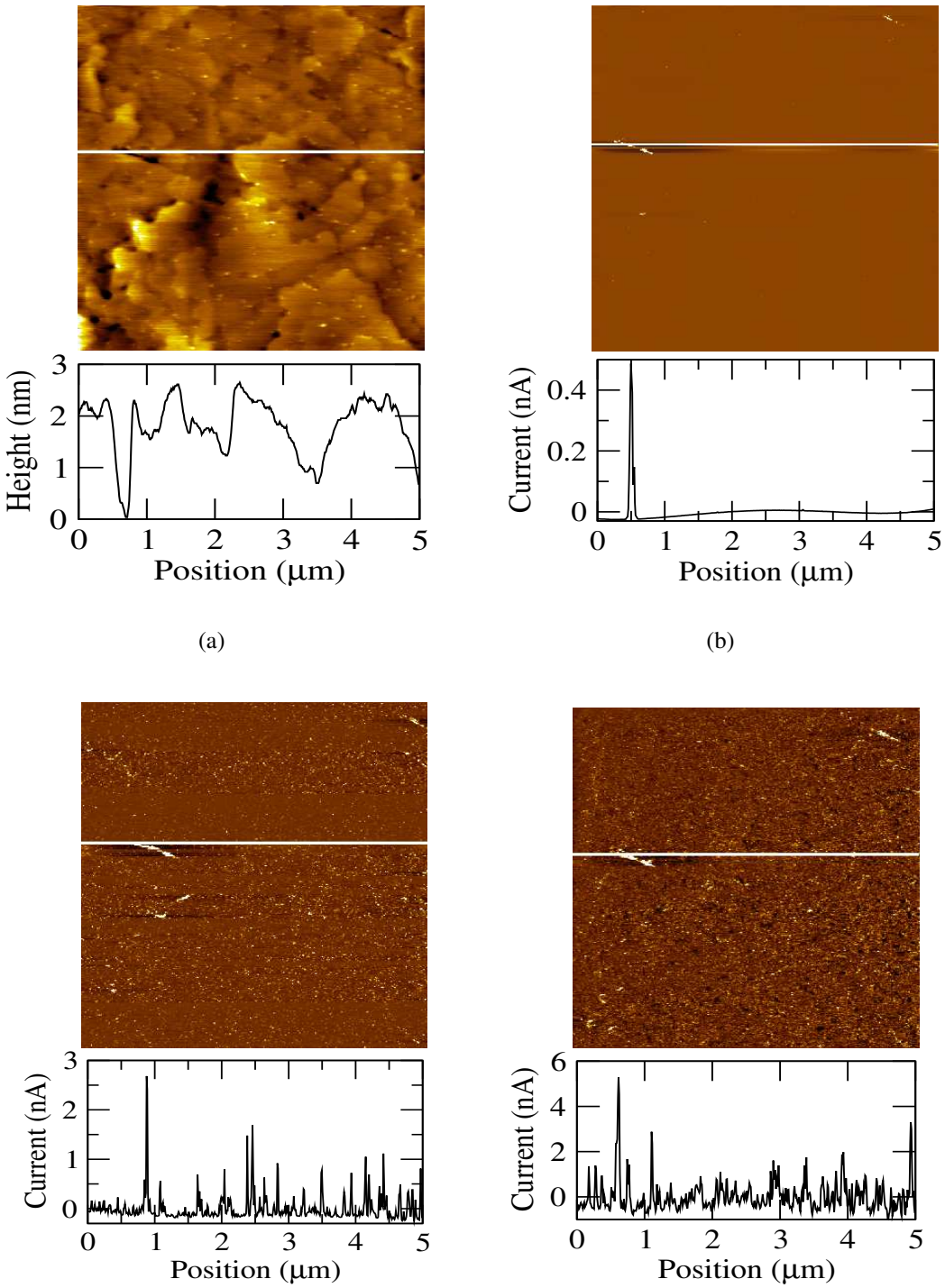

Figure 5.7: CS-AFM images of pure PyTp monolayer film on gold coated mica substrate at a constant force of 4 nN: (a) Topography. (b)Current image at 0.1 V sample bias. (c) Current image at 1 V sample bias. (d) Current image at 2V sample bias.

ranges. Figure 5.8 shows the simultaneously acquired topography and current images for pure PyTp monolayer film at a bias voltage of 2 Volts for a scan range of 1.5 × 1.5 μm^2. At this bias voltage, a current flow of about 1 nA was observed across the film [26]. The PyTp-DNA complex monolayer film formed on gold coated mica substrate was also imaged by CS-AFM. Figure 5.9 shows the topography and current images of the complex film at 0.5 V sample bias. The topography shows a film height of ∼ 3.2 nm. The current flow at this bias voltage was negligible except for the small void regions. The PyTp-DNA complex film exhibited appreciable conductivity only above 1 Volt sample bias.

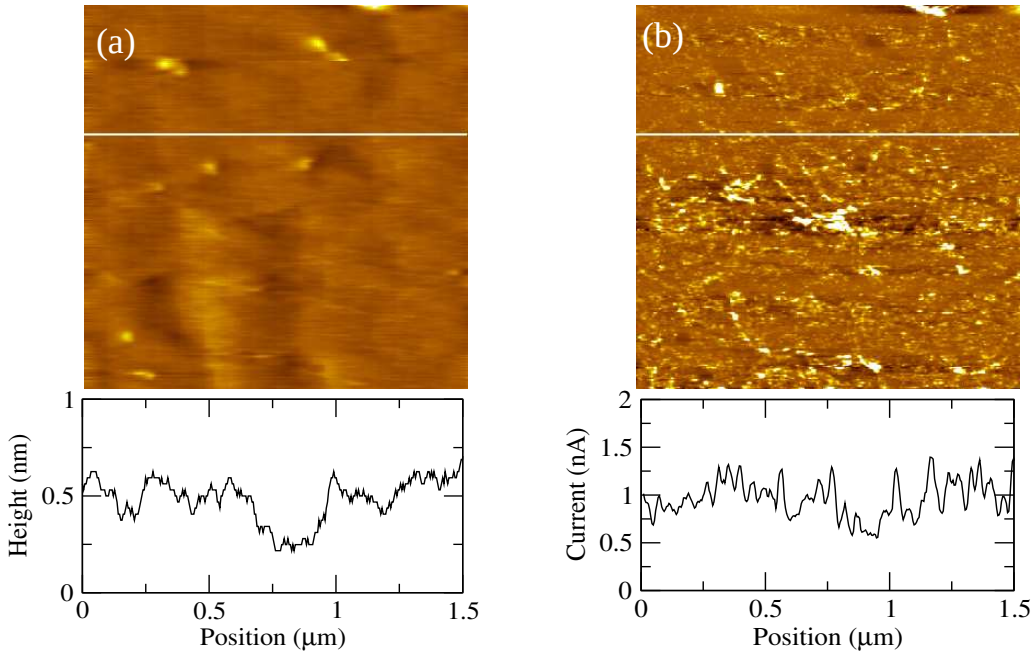

Figure 5.8: CS-AFM images of a smaller scan range for PyTp monolayer film on gold coated mica substrate at a sample bias of 2 V and a constant force of 4 nN: (a) Topography showing the surface roughness. (b) Current image showing the current flow of about 1 nA across the film surface.

In addition, we have carried out current imaging for the films prepared on polished doped silicon substrate. The rms value of roughness for bare silicon substrate was 0.06 nm (Figure 5.10). Figures 5.11(a) and 5.11(b) show the simultaneously acquired topography and current images for the complex film on doped silicon substrate at a sample bias of -7 Volts and at a constant force of 6 nN. We would like to mention that due to the presence of oxide layer on silicon substrates, the voltage required for current imaging was high. Such high voltages are also reported in literature for silicon with oxide layer [27]. Figure 5.11(c) shows the height and current profiles corresponding to

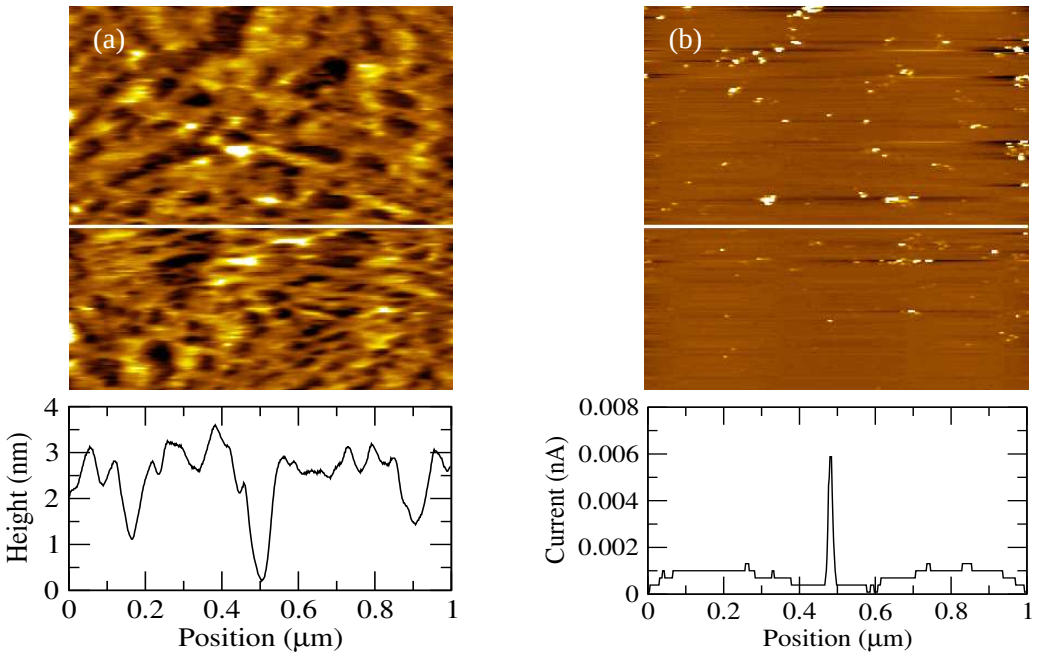

Figure 5.9: CS-AFM images for PyTp-DNA complex monolayer film on gold coated mica substrate at a sample bias of 0.5 V and a constant force of 4 nN: (a) Topography. (b) Current image.

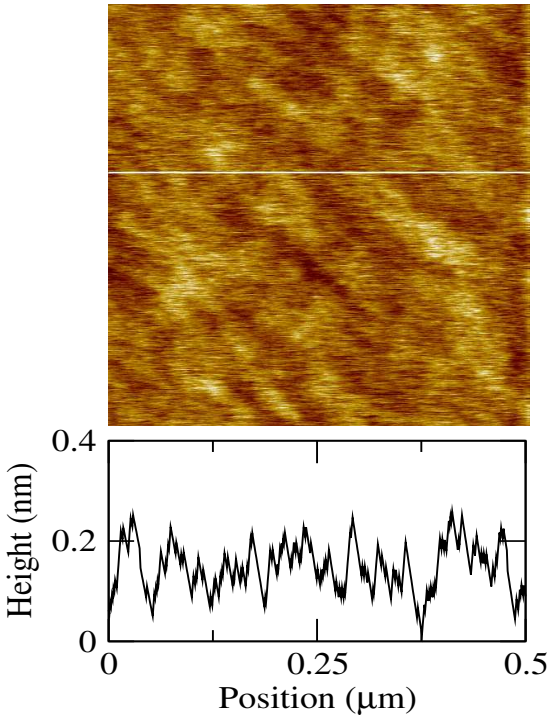

Figure 5.10: Topography image of a bare silicon substrate showing atomically flat surface with rms roughness of 0.06 nm.

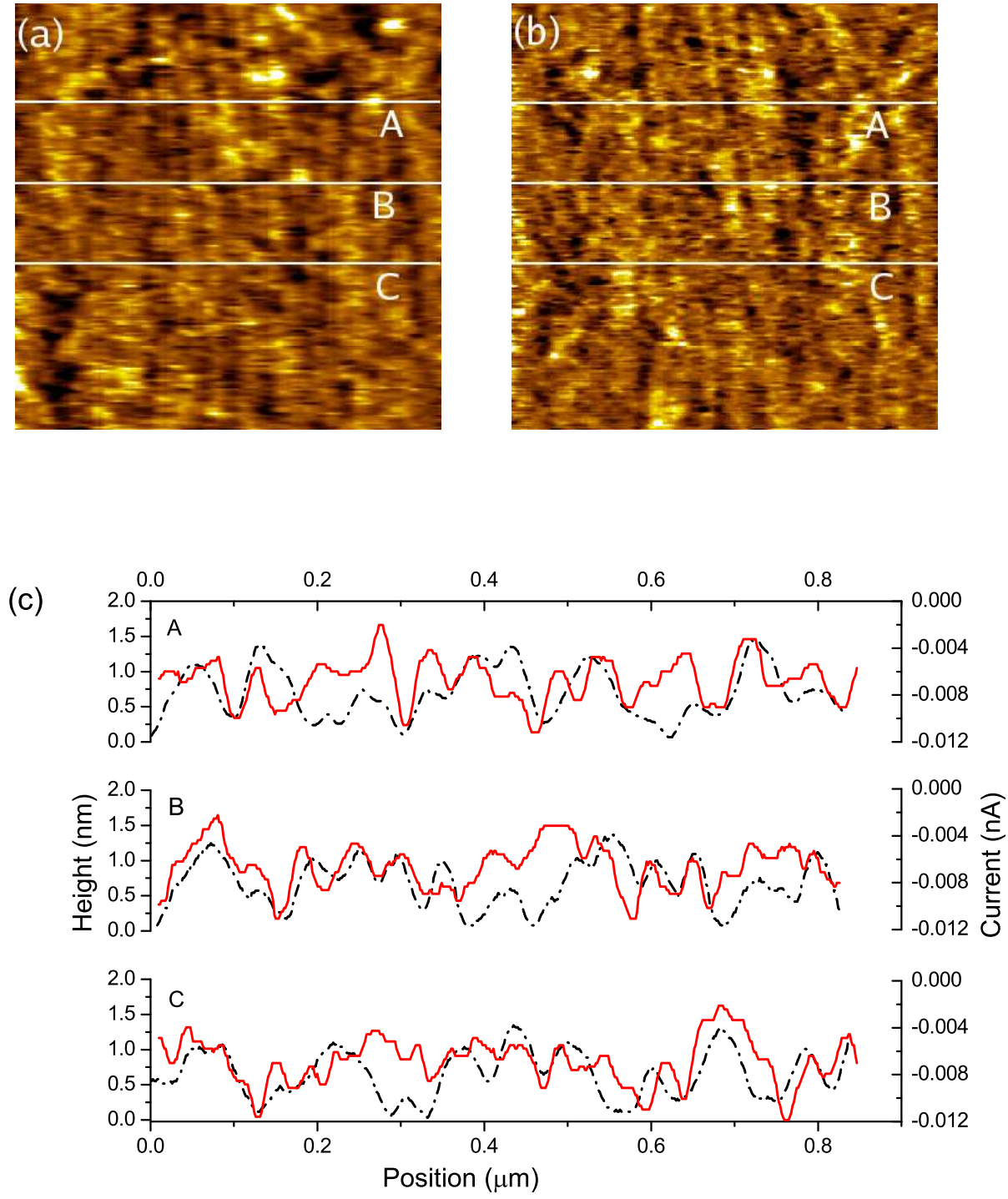

Figure 5.11: CS-AFM images for PyTp-DNA complex monolayer film on doped silicon substrate at a sample bias of -7 V: (a) Topography, (b) Current image. (c) The height (dash-dotted line) and current (continuous line) profiles corresponding to the lines drawn on the respective topographic and current images.

the lines drawn on the respective images. We have shown the profiles for three different positions on the film for better clarity. We find that the current values were about 0.004 nA at positions where the film thickness was high, whereas, they were about 0.01 nA at positions where the film thickness was low [26]. We have represented the current values in Figure 5.11(c) in negative scale in order to emphasize on the anti-correlation between the magnitude of the current and the height of the film. Thus, on a silicon substrate, which was atomically flat, it was possible to resolve this fine variation in current image due to the film only. Additionally, after performing current imaging in contact mode, we have again scanned the same region of the film in tapping mode to ensure no damage to the film.

5.4.2 *I-V* Spectroscopy

The current (I) - voltage (V) measurements were performed at various positions on both the pure and the complex films deposited on gold coated mica substrates. The I-V curves were acquired while the tip was held at a fixed position and the applied voltage ramp was from -3 to +3 Volts with a scan rate of 1 Hz. Representative I-V curves on pure film and complex film are shown in Figures 5.12(a) and 5.12(b) respectively. The tunneling current rapidly increased above a certain threshold voltage for both the films. For a given applied voltage, the magnitude of the current for PyTp film was significantly larger than that for PyTp-DNA complex film. With an applied bias of 1 Volt, the average electrical currents through pure PyTp and PyTp-DNA complex films were 0.2 nA and 0.05 nA, respectively. In both the cases, forward and reverse currents are found to offset by small values (10 - 14 pA) from the zero current line due to the charging current of the system capacitance [28]. We have observed a positive offset for an increasing voltage ramp and a negative offset for a decreasing voltage ramp.

To identify different transport regimes depending on the applied bias, it is important to represent the I-V curves in log-linear scale. Figures 5.13(a) and 5.14(a) show the log-linear representation of typical I-V characteristics for the pure and complex films, respectively. We find that, for both the films, the log-linear representation of I-V curves did not show any indication of the existence of different transport regimes. In Figures 5.13(b) and 5.14(b), we have shown the Fowler-Nordheim (FN) plots of $\ln(I/V^2)$ against $1/V$ constructed from the respective I-V curves for the pure and

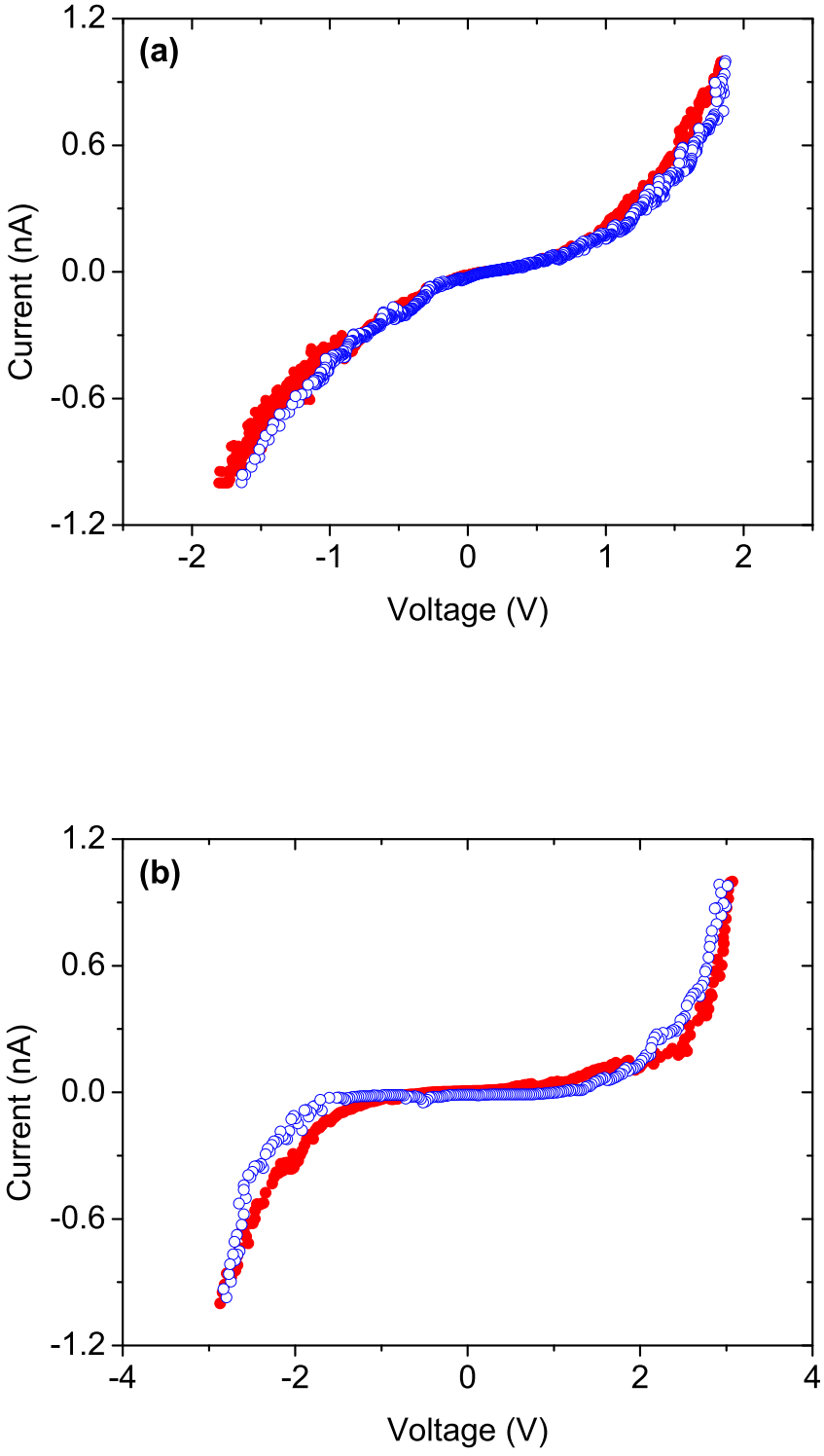

Figure 5.12: Typical *I-V* characteristics measured by CS-AFM on monolayer films of (a) PyTp and (b) PyTp-DNA complex, on gold coated mica substrates at a constant force of 4 nN. The solid circles represent forward voltage scan and the open circles represent reverse voltage scan.

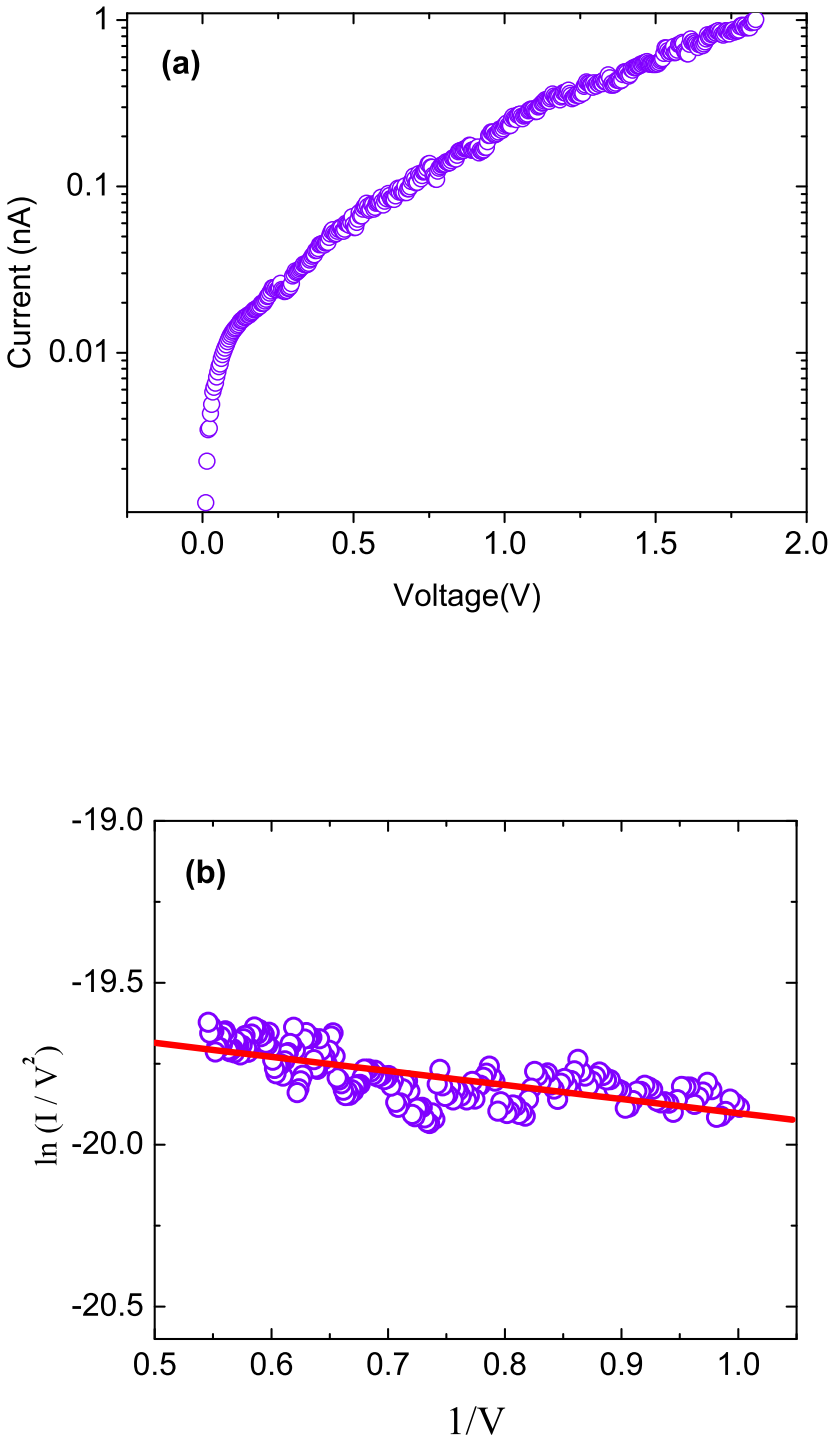

Figure 5.13: (a) Log-linear representation and (b) Fowler-Nordheim fitting for a typical *I-V* characteristic curve measured for the pure PyTp monolayer film on a gold coated mica substrate at a constant force of 4 nN. Open circles represent the experimental data and solid line represents the fit.

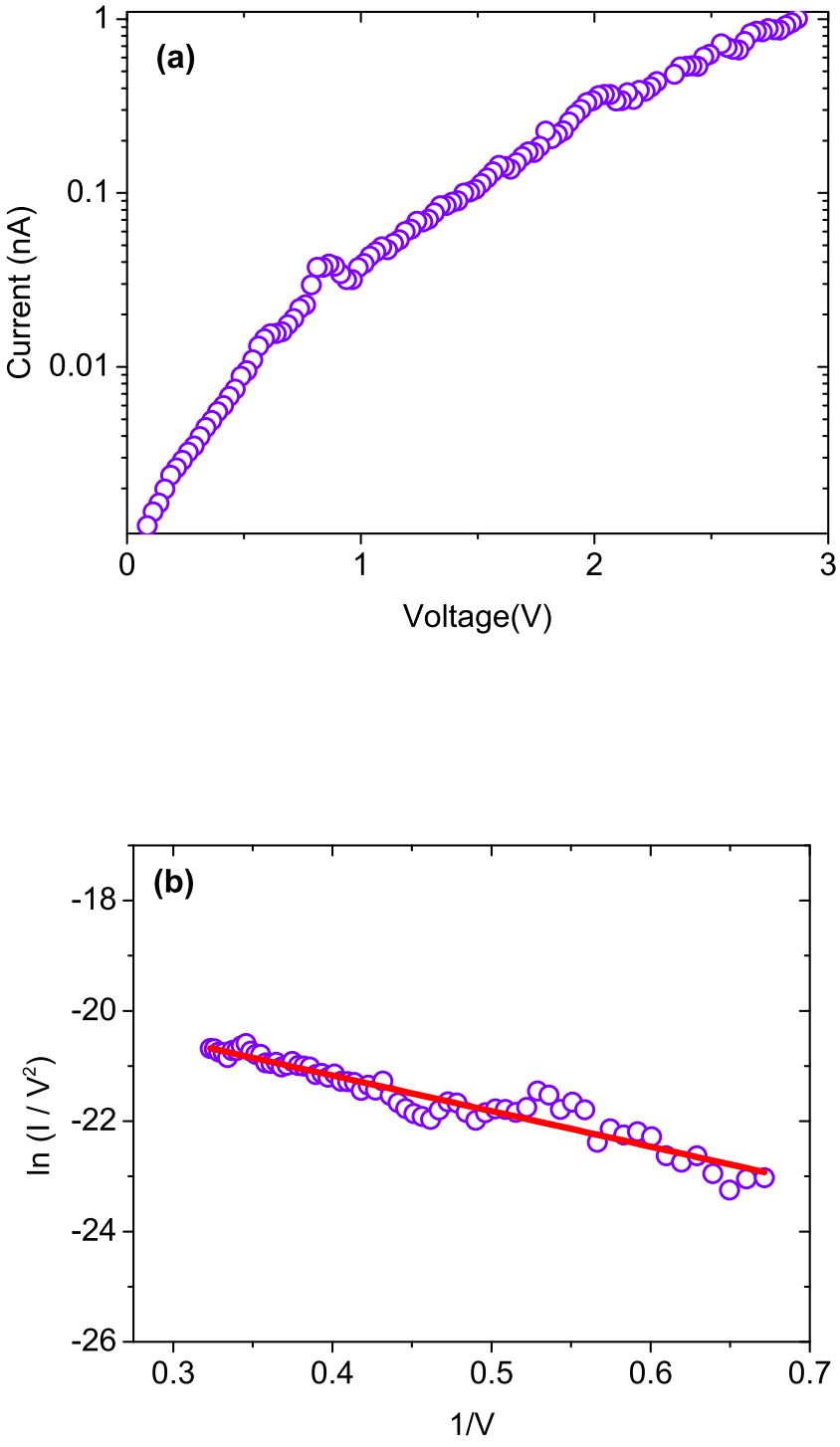

Figure 5.14: (a) Log-linear representation and (b) Fowler-Nordheim fitting for a typical *I*-*V* characteristic curve measured for the PyTp-DNA complex monolayer film on a gold coated mica substrate at a constant force of 4 nN. Open circles represent the experimental data and solid line represents the fit.

complex films. The FN plot shows a straight line whose slope yields the B value. The open circles represent the experimental data points and the solid line represents the fit. We find that the I-V data for both the films fit well with this model. It is to be noted that FN is an approximation in the high voltage regime [24]. Therefore, we have shown the fitting of our data for the high voltage regime only.

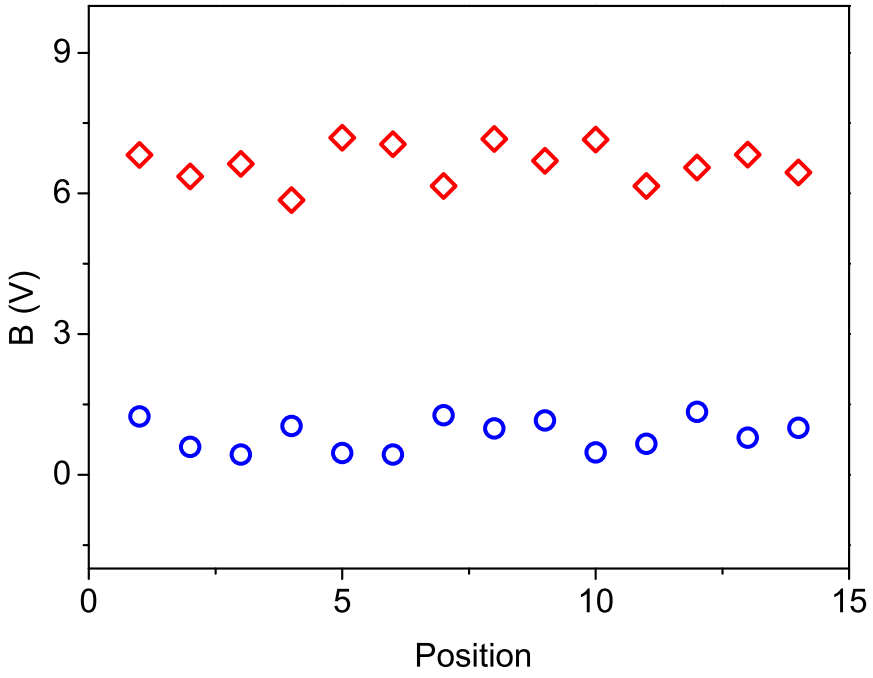

Figure 5.15: The B values obtained from the FN plots of the I-V curves measured at 14 different positions on PyTp monolayer (○) and PyTp-DNA complex monolayer (◇) films. The average B value is 0.85 Volt for the pure film and 6.6 Volts for the complex film.

We have obtained several I-V curves at different positions on the films and fitted them with the FN model. Figure 5.15 shows the B values obtained for 14 such I-V curves measured at different positions on the pure and complex films. The average B value obtained from Figure 5.15 was 0.85 Volt for the pure film and 6.6 Volts for the complex film. Using these B values and the corresponding film thicknesses (2.2 nm for PyTp film and 3.2 nm for PyTp-DNA complex film) in equation 5.14, we have calculated the barrier heights ϕ_b to be $0.15(m/m^*)^{1/3}$ eV and $0.45(m/m^*)^{1/3}$ eV for the pure and complex films respectively [26].

5.5 Discussion

We have studied the electrical conductivity of LB films of pure PyTp as well as PyTp-DNA complex. Prior to performing the measurements on these LB films, we have tested the conductivity of the current-sensing AFM tip. The *I*-*V* curve measured with the platinum coated tip on a bare gold surface gave a contact resistance of nearly 100 MΩ (Figure 5.5). This high value for contact resistance might be due to a thin layer of moisture on the surface of the substrate, which is likely since the measurement was carried out in ambient conditions and the gold surface is hydrophilic. However, the LB film surfaces of both PyTp and PyTp-DNA complex, being hydrophobic, are expected to be less affected by moisture layer compared to a bare gold surface. In addition, the contact resistance depends on the contact force between the tip and sample. The contact resistance can decrease by several orders of magnitude by increasing the contact force. But increasing the contact force may damage the film. Therefore, we have selected the contact force carefully such that there was no film damage, and at the same time, we could get appreciable amount of current.

We have obtained current images for both the pure and complex LB films (Figures 5.7, 5.8 and 5.9). We find that the PyTp-DNA complex film needs more bias voltage to generate a current flow as compared with the pure PyTp film indicating the complex film to be more resistive. The inhomogeneities observed in the current image (Figure 5.8(b)) might be due to the defects in the gold coating on mica substrate. Similar inhomogeneities were also observed for bare gold film on mica. Further, the probe works in contact mode in our methodology. The effects of contact forces are ; slight compression of the film and the change in the contact area itself due to the film surface roughness. These are also possible reasons for current inhomogeneities. Such inhomogeneities in current images are also reported in literature for organic films [17, 20].

In addition to the current imaging on gold surface, we have carried out current imaging on polished doped silicon substrate. The polished silicon substrate, being atomically flat, elucidates the actual topographical variation in the film surface, whereas, on a gold surface which is rough compared to a polished silicon surface, such variations are difficult to observe. The bare silicon substrate exhibits atomically flat surface (Figure 5.10). The pure PyTp film on the polished silicon substrate showed a smooth film surface with a rms value of roughness of ~ 0.2 nm (Figure 2.8(b),

Chapter 2). For PyTp-DNA complex film, the phase imaging in tapping mode performed with a super sharp probe with tip radius of ~ 2 nm yielded a high spatial resolution image of the surface (Figure 4.6, Chapter 4). With a super sharp tip, the topography image of the complex film revealed a compact film surface, whereas, the corresponding phase image clearly resolved a periodic structure with a periodicity of ~ 36 nm. As discussed in the previous chapter, this periodic structure corresponds to the DNA bundles aligned in the film deposition direction. Since it was possible to resolve the periodic structure due to the presence of DNA in the film on the polished silicon surface, we have performed current imaging on the same film to understand the role of DNA in modifying the conductivity of the film. For current imaging, we have used conducting probe with a tip radius of ~30 nm. It is known that the spatial resolution of measurements is limited by the end radius of the probe. Since the radius of the conducting tip is comparable to that of the periodicity on the complex film surface, the current sensing AFM tip (radius ~ 30 nm) senses this periodic variation as can be seen in Figure 5.11(a) but not as clearly as it was sensed by the super sharp tip with radius of ~2 nm. Therefore, the minimum height sensed by the current-sensing AFM tip does not correspond to the actual depth where there is no DNA on the periodic surface. However, the conductive tip senses a variation in current flow across the film. This variation in conductivity revealed in the current image (Figure 5.11(b)) may be attributed directly to the topographical variations in the film surface itself since the probe works in the contact mode. Interestingly, we find anti-correlation between the magnitude of the current and the film height as shown in Figure 5.11(c). The current values were low at positions where the film thickness was high [26]. This indicates that the presence of DNA modifies the conductivity of the film. On the basis of these results, we have drawn a cartoon representing the PyTp-DNA complex film structure on polished silicon surface (Figure 5.16).

Although current imaging can provide conductivity map of a film surface, a wealth of information on the charge transport properties can be extracted from the current (I) - voltage (V) characteristics. We have performed I-V spectroscopy on both the pure and the complex films deposited on gold coated mica substrates. We have analyzed the I-V curves to explore the possible mechanism for the electron transport in our system. The metal substrate, the LB film and the conducting tip

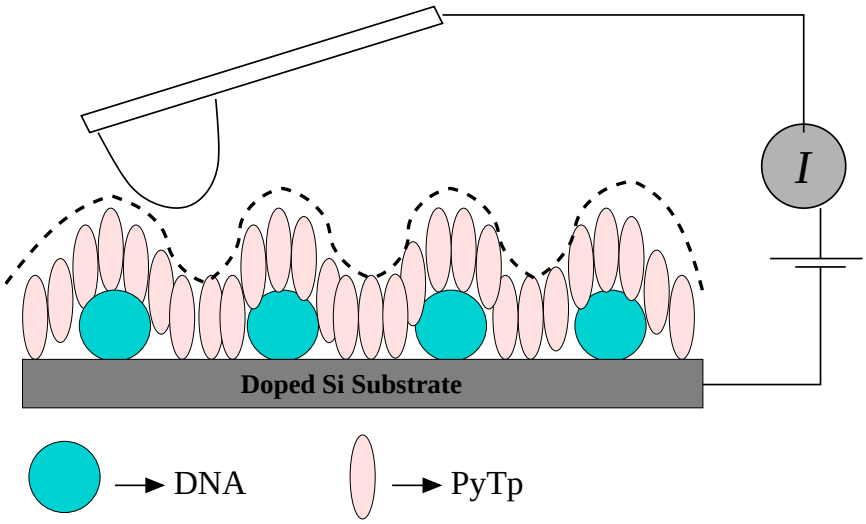

Figure 5.16: Cartoon representation of the PyTp-DNA complex monolayer film on polished doped silicon substrate. The conducting AFM tip senses less current at positions with higher film thickness and more current at positions with lower film thickness, thereby revealing the current variation in the film.

form a nanoscopic metal-insulator-metal (M-I-M) junction. For both the films, the shape of the *I*-*V* curves measured for such junction strongly suggests a barrier for electron transport at the tip-sample interface. The barrier height at the interface is an important parameter for electron transfer across the interface. One can choose appropriate model to describe the measured *I*-*V* curves and to determine the barrier height between the film and the metal substrate. We have considered two basic mechanisms for electron transport; thermionic (schottky) emission and electron tunneling. In the thermionic emission model for a M-I-M junction, the derivative dI/dV decreases with increasing current (Section 5.3.1.1). We find that the derivative dI/dV increases with increasing current in our *I*-*V* curves (Figure 5.12). Therefore, Schottky emission is not a possible mechanism for current transport through the metal-LB film-metal junction. The nature of our *I*-*V* curves suggests that the electron tunneling might be a possible mechanism for electron transport in our system. For interpreting electron tunneling, the FN tunneling model is widely used [28, 29]. The FN model is an approximation in high voltage regime (V> ϕ_b/e). In the low voltage regime, direct tunneling is known be dominant. These are discussed in the theory section (Section 5.3) of this chapter. To identify the different transport regimes based on the applied bias voltage, it is necessary to represent the *I*-*V* curves in log-linear scale. In recent reports by Casuso et al. [30] and Beebe et al. [31], a transition from direct tunneling to injection (FN) tunneling was observed. The log-linear rep-

resentation of the *I-V* curves in these two reports clearly indicated the transition between the two regimes. However, in our system, we did not observe an indication of a transition in the log-linear representation of the *I-V* characteristics for both the films (Figures 5.13(a) and 5.14(a)). We have fitted our *I-V* data with the FN model and find that, for both the films, the correlation between the data and the fit was better than 98%. At lower voltages, the system charging effect, thermal and Schottky effects become dominant which prevents us from extracting any meaningful information at that regime. On the basis of the analysis of our *I-V* curves, and within the experimental limits, we find FN to be a possible mechanism for electron transport in our system [26].

Further, we have used the FN plot to determine the barrier height for the films. The FN plot yields a straight line whose slope (B) and intercept (A) depend on the barrier height (Figures 5.13(b) and 5.14(b)). To calculate the barrier height from the A and B values, we need the values of effective area (A_{eff}) and effective mass of electron (m^*) (Equations 5.13 and 5.14). It was highlighted by Casuso et al. that the presence of two different transport regimes in their system made it possible to measure m^* and A_{eff}. In our system, we did not observe any such transition. Hence, it was not possible for us to determine m^* and A_{eff}. Moreover, the tip operates in the contact mode. Hence, it may suffer from various local inhomogeneities arising due to sample morphology and local interaction forces. These effects make the measurement of A_{eff} to be very difficult and hence, conclusions drawn by using any assumed A_{eff} to calculate barrier height will not be correct. Consequently, the A value (equation 5.13) was not very useful in our case. We have used the B value (equation 5.14) where m^* is the only unknown parameter for extracting the barrier heights. For similar reasons, when it is difficult to calculate A_{eff} and m^*, researchers generally use B value to extract the barrier height [32]. Using the average B values obtained from various *I-V* curves measured at different positions on the films, we have obtained the barrier heights to be $0.15(m/m^*)^{1/3}$ eV and $0.45(m/m^*)^{1/3}$ eV for the pure and complex films respectively [26].

In literature, direct tunneling is known to be dominant for alkyl systems [33], due to their large highest occupied molecular orbital - lowest unoccupied molecular orbital (HOMO-LUMO) gaps (~8 eV). Direct tunneling refers to nonresonant tunneling (electrons tunnel directly from metal to metal) that occurs when the applied bias voltage is less than the barrier height. In contrast to the

alkyl system, the mechanism of charge transport in a junction containing π-conjugated molecules is different. For π-conjugated species, the decreased HOMO-LUMO gap increases the likelihood of injection tunneling. Injection tunneling refers to resonant tunneling (electrons are injected first into the insulator and then arrive to the second electrode) which occurs in the Fowler-Nordheim regime ($V > \phi_b/e$). Recently, Beebe et al. have observed a transition from direct tunneling ($V < \phi_b/e$) to injection tunneling ($V > \phi_b/e$) for π-conjugated systems [31]. However, in our system direct tunneling may not be feasible. For disk-shaped liquid crystals, the packing and supramolecular order, which depends on their chemical structure in a non-predictable manner, drastically influences the electronic properties [1]. Hence, clear-cut structure-property relationship is not directly accessible. In a recent quantum-chemical calculation, it has been illustrated that when discotic molecules are arranged in a columnar stack, a quasi-band structure forms with Bloch-like orbitals delocalized over several molecules in the column [34]. In our system, the PyTp molecules in the LB films are arranged in columns. It appears that due to the overlap of molecular orbital wave functions, a quasi-band structure might have formed with a very small band gap. Our FN fitting results also suggest that for the pure film the barrier height may be as low as 0.15 eV.

For PyTp-DNA complex system, we find that the presence of DNA leads to further barrier to electron transport. But it is difficult to quantify or comment on the conductivity of DNA molecules alone from such an experiment. The higher barrier height in the complex film is likely to be a direct consequence of change in packing of the molecules. The conformation of DNA molecule and the environment in which it is present have a crucial impact on its conductivity [11]. On the basis of our observations, we find that complexation with DNA makes the film more resistive. However, a complete quantitative understanding of the type of electron transport needs detailed information about the electronic structure of the system.

5.6 Conclusions

We have studied the nanoscale electrical conductivity of Langmuir-Blodgett films of PyTp monolayer and PyTp-DNA complex monolayer by current-sensing atomic force microscopy. We find that the *I-V* curves fit well with the Fowler-Nordheim (FN) tunneling model indicating the electron

tunneling to be a possible mechanism for electron transport. Further, analysis of the *I-V* curves based on the FN model yields the barrier height of PyTp-DNA complex film to be three times higher compared to that of the pure PyTp film. The local electrical conductivity measurement of the films using CS-AFM provides better understanding of the electron transport properties at the nanoscale.

In the previous chapters, we have shown the organization of ionic discotic molecules at the air-water and air-solid interfaces, together with their complexation with DNA. We have studied the mechanical and electrical properties of these films at nanoscale and have shown how complexation with DNA modifies the film properties. In all these studies, the constituent discogen molecule was a *monomer*. It is known in literature that the properties exhibited by a discotic *dimer* can be significantly different from the conventional low molar mass discotic monomers because of the restricted molecular motions [35]. We explore, in the next chapter, the organization of a discotic *dimer* (i.e., two discotic monomers connected by a polar moiety) at interfaces, together with its complexation with DNA.

Bibliography

[1] S. Sergeyev, W. Pisula, and Y. H. Geerts, *Chem. Soc. Rev.* **36**, 1902 (2007).

[2] C. M. Gordon, J. D. Holbrey, A. R. Kennedy, and K. R. Seddon, *J. Mater. Chem.* **8**, 2627 (1998).

[3] Alpana Nayak, K. A. Suresh, Santanu Kumar Pal, and Sandeep Kumar, *J. Phys. Chem. B* **111**, 11157 (2007).

[4] M. Yoshio, T. Mukai, H. Ohno, and T. Kato, *J. Am. Chem. Soc.* **126**, 994 (2004).

[5] Alpana Nayak and K. A. Suresh, *J. Phys. Chem. B* **112**, 2930 (2008).

[6] W. Pisula *et al.*, *Adv. Mater.* **17**, 684 (2005).

[7] J. J. Gooding and G. C. King, *J. Mater. Chem.* **15**, 4876 (2005).

[8] G. B. Sukhorukov, M. M. Montrel, A. I. Petrov, L. I. Shabarchina, and B. I. Sukhorukov, *Biosensors and Bioelectronics* **11**, 913 (1996).

[9] D. Porath, A. Bezryadin, S. de Vries, and C. Dekker, *Nature* **403**, 635 (2000).

[10] L. Cai, H. Tabata, and T. Kawai, *Appl. Phys. Lett.* **77**, 3105 (2000).

[11] R. G. Endres, D. L. Cox, and R. R. P. Singh, *Rev. Mod. Phys.* **76**, 195 (2004).

[12] D. D. Lasic and N. S. Templeton, *Advanced Drug Delivery Reviews* **20**, 221 (1996).

[13] Y. Okahata, T. Kobayashi, K. Tanaka, and M. Shimomura, *J. Am. Chem. Soc.* **120**, 6165 (1998).

[14] L. Cui, J. Miao, and L. Zhu, *Macromolecules* **39**, 2536 (2006).

[15] G. V. Nazin, X. H. Qiu, and W. Ho, *Science* **302**, 77 (2003).

[16] N. P. Guisinger, N. L. Yoder, and M. C. Hersam, *Proc. Natl. Acad. Sci. U.S.A* **102**, 8838 (2005).

[17] X. D. Cui *et al.*, *Nanotechnology* **13**, 5 (2002).

[18] M. Freitag, M. Radosavljevic, W. Clauss and A. T. Johnson, *Phys. Rev. B* **62**, R2307 (2000).

[19] I. Casuso, L. Fumagalli, J. Samitier, E. Padros, L. Reggiani, V. Akimov, and G. Gomila, *Nanotechnology* **18**, 465502 (2007).

[20] D. -H. Han, J. -W. Kim, and S. -M. Park, *J. Phys. Chem. B* **110**, 14874 (2006).

[21] J. Reichert, R. Ochs, D. Beckmann, H. B. Weber, M. Mayor, and H. v. Lohneysen, *Phys. Rev. Lett.* **88**, 176804 (2002).

[22] D. J. Wold and C. D. Frisbie, *J. Am. Chem. Soc.* **122**, 2970 (2000).

[23] S. M. Sze, *Physics of Semiconductor Devices*, 2nd Edition, John Wiley and Sons: New York, (1981).

[24] J. G. Simmons, *J. Appl. Phys.* **34**, 1793 (1963).

[25] M. Lenzlinger and E. H. Snow, *J. Appl. Phys.* **40**, 278 (1969).

[26] Alpana Nayak and K. A. Suresh, *Phys. Rev. E* **78**, 021606 (2008).

[27] A. Olbrich, B. Ebersberger, and C. Boit, *Appl. Phys. Lett.* **73**, 3114 (1998).

[28] P. Mishra, P. Karmakar, and D. Ghose, *Nucl. Instr. Meth. Phys. Res. B* **243**, 16 (2006).

[29] K. Yano *et al.*, *Appl. Phys. Lett.* **68**, 188 (1996).

[30] I. Casuso *et al.*, *Phys. Rev. E* **76**, 041919 (2007).

[31] J. M. Beebe, B. S. Kim, J. W. Gadzuk, C. D. Frisbie, and J. G. Kushmerick, *Phys. Rev. Lett.* **97**, 026801 (2006).

[32] D. Xu, G. D. Watt, J. N. Harb, and R. C. Davis, *Nano Lett.* **5**, 571 (2005).

[33] W. Wang, T. Lee, and M. A. Reed, *Phys. Rev. B* **68**, 035416 (2003).

[34] X. Crispin *et al.*, *J. Am. Chem. Soc.* **126**, 11889 (2004).

[35] Sandeep Kumar *Chem. Soc. Rev.* **35**, 83 (2006).